



Tensile strength of hydrated cement paste phases assessed by micro-bending tests and nanoindentation



J. Němeček^{a,*,1}, V. Králík^{a,2}, V. Šmilauer^{a,3}, L. Polívka^{b,4}, A. Jäger^{b,5}

^a Czech Technical University in Prague, Faculty of Civil Engineering, Department of Mechanics, Thákurova 7, 166 29 Prague 6 Czech Republic

^b Laboratory of Nanostructures and Nanomaterials, Institute of Physics of ASCR, Na Slovance 2, 182 21 Prague 8, Czech Republic

ARTICLE INFO

Article history:

Received 14 October 2015

Received in revised form

1 July 2016

Accepted 15 July 2016

Available online 18 July 2016

Keywords:

Cement

Hydration products

Micro-beam

Tensile strength

Fracture energy

Nanoindentation

Focused ion beam

ABSTRACT

The paper is focused on the experimental investigation of cement paste's tensile strength and related mechanical properties at the micrometer level. Small scale specimens with micrometer dimensions in the form of cantilever beams having a triangular cross section and $\approx 20 \mu\text{m}$ in length are fabricated by means of a focused ion beam and tested in bending with the aid of a nanoindenter. Elastic properties are evaluated from both bending and nanoindentation tests for all the phases with very close agreement. The phase separation is performed with SEM-based image analysis and the deconvolution of grid nano-indentation results. The load-deflection curves of bent beams are monitored up to the failure for distinct microlevel phases, namely for inner and outer products and Portlandite. The tensile strength of the phases is directly derived from the load-deflection curves in the range of 264 MPa (for the outer product) to 700 MPa (for the inner product and Portlandite). Moreover, the load-deflection curves are used for the supremum estimates of fracture energies for individual hydrated cement phases. Low values of the energies in the range of $4.4 - 20 \text{ J/m}^2$ were found. The values obtained experimentally in this paper correspond well with those published in recent multiscale or molecular dynamics models.

© 2016 Published by Elsevier Ltd.

1. Introduction

Concrete is the most widespread civil engineering material in the world. The main binding component of this composite material is Portland clinker, which can be blended with slag, fly-ash, calcium carbonate, microsilica and other supplementary materials that serve as fillers and/or pozzolanic reactants [1]. Other components include water, aggregates and a variety of possible admixtures such as fibers. Concrete is also a composite with a hierarchical microstructure that comes both from the mixture of different components and from hydration reactions that evolve in time. Its mechanical properties are largely affected by various factors at all composite levels. The most important ones include the initial

binder type, inclusions type and content, the air void content and the extent of interfacial zones between individual phases. To reduce the complexity of the material microstructure, concrete is usually treated with multi-scale models that must span over a range of levels starting from nanometers to meters [2–4].

At the microlevel, the main binding component, i.e. the hydrated cementitious matrix, is composed of a few main constituents: hydration products (known from cement chemistry as Calcium-Silica-Hydrates, labeled hereafter as C-S-H gels; other hydrates, e.g. ettringite-AFt, monosulfate-AFm, Calcium-Aluminate-Hydrates (C-A-H); Portlandite $\text{Ca}(\text{OH})_2$ (labeled as CH); porosity; anhydrous clinker minerals and some other minor (mechanically insignificant) phases [1,5,6].

Concrete is used due to its many advantages that include practicality (e.g. easy shaping, local availability of source materials), economical issues (i.e. its relative low-cost compared to other materials like metals), very good mechanical properties (e.g. high stiffness, high compressive strength) and durability.

One of the weak points of concrete is its relatively low tensile strength (typically a few MPa). However, the theoretical strength of quasibrittle materials increases as the sample size or scale decreases. This is valid for finer scales (nano- and micrometer), where

* Corresponding author.

E-mail addresses: jiri.nemecek@fsv.cvut.cz (J. Němeček), vlastimil.kralik@fsv.cvut.cz (V. Králík), vit.smilauer@fsv.cvut.cz (V. Šmilauer), polivka@fzu.cz (L. Polívka), jager@fzu.cz (A. Jäger).

¹ Assoc. Prof. Ing. Jirí Ing. Němeček, Ph.D.

² Ing. Vlastimil Králík, Ph.D.

³ Assoc. Prof. Ing. Vít Smilauer, Ph.D.

⁴ Ing. Leoš Polívka.

⁵ RNDr. Aleš Jäger, Ph.D.

previous modeling showed the tensile uniaxial strength of low- and high-density C-S-H phases to be $C-S-H_{LD} = 66$ MPa and $C-S-H_{HD} = 107$ MPa and for the C-S-H globule to be as high as 320 MPa [7,8]. Since such tensile strengths have never been measured experimentally on finer scales, the purpose of this work is to directly measure them on individual components of hydrated cement paste. This is achieved by fabricating small cantilevers by the Focused Ion Beam technology, FIB, and performing direct bending tests with the aid of a nanoindenter. This pioneering work offers new insights into the material strength origin and gives valuable quantitative information for numerical models that need to be calibrated on finer scales.

By now, the mechanical quantification of microlevel components has been provided almost exclusively by nanoindentation [9]. This technique allows penetrating specimen's surface by a sharp indenter leading to the evaluation of mechanical information from shallow depths, typically below 1 μm on cement components. Nanoindentation has been successfully used to assess the elastic stiffness of individual phases at the submicron level of cement paste. The elastic moduli of anhydrous clinker minerals were measured, for example, by Velez et al. [10] and Nemeček [11]. The elastic moduli of C-S-H phases in two characteristic densities [12], low- and high-density C-S-H gels, were firstly reported by Constantinides and Ulm [13] and confirmed by other researchers on various cementitious systems, e.g. Refs. [11,14,15]. The elastic stiffness of individual cement components was studied in conjunction with calcium leaching providing the evidence of two characteristic C-S-H densities [13]. Nanoindentation was employed to extract, for example, the phase elastic properties of various heterogeneous systems [16], high performance concretes [4] and interfacial transition zones [17]. The grid indentation technique is usually used to deal with the statistical heterogeneity of the cementitious matrix [16,18–20]. The papers so far have mentioned the use of mechanical polishing to prepare the surface of samples for indentation and the spatial resolution of measured mechanical properties is kept within a few hundred nanometers. Local mechanical characterization is also provided with a higher resolution by peak-force tapping AFM on a FIB-prepared specimen surface [21].

Nanoindentation can also be used as a versatile tool to load small scale specimens that are fabricated by either mechanical means or by FIB on micron or submicron levels. Typically, the micro-pillar or micro-beam geometry is prepared by FIB and the nanoindenter serves as a compression tool. This technique is used in material science (applied mostly to metals, various thin films and electronics components) to study the basic deformation mechanisms and behavior of small material volumes and to derive elastic, plastic and fracture material properties [22,23]. An application of a precision saw cutting for fabrication of micro-pillars in cement paste, subsequent nanoindentation and modeling of the failure mechanism can be found in Ref. [24]. The paper describes breaking of pillars without assessment of strength or breaking load. So far, however, the compression of micro-pillars or micro-bending tests have rarely been used in cementitious materials due to technical and instrumental demands. The first attempt to use FIB milling on cement paste and to quantify its strength from micro-machined beams was published by Chen et al. [25]. The authors presented an early data received from a single FIB-milled cantilever in cement paste loaded with AFM. They found the flexural strength of cement paste to be as low as 2.67 MPa which seems to be in contradiction to scaling of strength to micrometers in quasi-brittle materials [26].

In this work, the micro-bending tests of FIB prepared samples were adopted and individual cement paste phases quantified for the first time with the nanoindenter. A much larger extent of the measurements and information on phases' elasticity, tensile strength and fracture properties is presented in this paper.

2. Materials and methods

2.1. Cement paste

Hydrated cement paste samples were prepared from Portland cement CEM-I 42,5R (taken from the Heidelberg cement plant in Mokrý, Czech Republic). The chemical composition of the cement is shown in Table 1. The fineness of the cement, characterized by the Blaine specific surface, was $306 \text{ m}^2 \text{ kg}^{-1}$. The cement was mixed with water to yield a water/cement ratio of 0.4, stirred and vibrated to release entrapped air. The mixture was poured into small cylindrical plastic moulds (height = 60 mm, diameter = 30 mm). The next day after casting, the samples were demoulded, placed into tanks with water and stored. The storage time was 7 years at an average laboratory temperature of 22°C . After such a long time, a very high degree of hydration can be anticipated meaning the paste contains a minimum amount of anhydrous components.

Before testing, the samples were cut into 5 mm thick slices by a precision diamond saw, dried in ambient conditions (with the relative humidity below 40%) and mechanically polished with a series of SiC papers down to the grit size #4000 in the Struers[®] metallographic polishing system. Then, the samples were observed with the Scanning Electron Microscope (SEM) for the volumetric quantification of individual material phases and micromachined with FIB. The samples were stored in an inert environment (Argon gas) to suppress carbonation between the tests.

2.2. Preparation of micro-beams by FIB

FIB was chosen to fabricate cantilever micro-beam specimens from cement paste samples. This technique allows precise shaping of the material at the microscale with physical limitations caused by the inaccessibility of some surfaces to the ion beam and possible redeposition of the sputtered material in a confined space. For these reasons, rectangular cross sections of the beams are not technically feasible and a triangular cross-section was chosen as the best geometry for micro-machining via FIB. The characteristic cross sectional depth of the beams was chosen to be around 3 – 4 μm while the cantilever length was around 20 μm . Such dimensions allow precise fabrication without defects or FIB artifacts and are still small enough to be produced within a single material phase. The ratio of length to transverse dimensions is approximately 5 in order to minimize the shear effect and to be able to deform the cantilever mostly in pure bending. The scheme of the beam geometry and loading direction is depicted in Fig. 1.

All micro-beams were prepared by the FEI Quanta 3D FEG dual beam instrument combining SEM and FIB. The FIB is a well-established technique that uses a finely focused beam of gallium ions for precise micromachining of various materials [27]. FIB milling procedure was optimized to suppress the redeposition of sputtered material on the micro-beam surface [28]. The final milling step was done at an accelerating voltage of 30 kV and a current of 1 nA. After FIB milling, the micro-beams were observed by SEM to verify their dimensions. Simulations carried out by SRIM 2013 [29] revealed that Ga^+ ions accelerated to 30 kV penetrate into the cement paste ≈ 36 nm deep on average. This introduces an affected layer $\approx 1\%$ of a micro-beam depth. Therefore, the influence

Table 1

Chemical composition of the used cement (XRD data supplied by the manufacturer).

Component	CaO	SiO ₂	Al ₂ O ₃	Fe ₂ O ₃	MgO	TiO ₂
wt %	63.77	20.51	4.74	3.3	1.05	0
Component	K ₂ O	Na ₂ O	SO ₃	MnO	free Ca	
wt %	0.95	0.15	3.07	0.09	0	

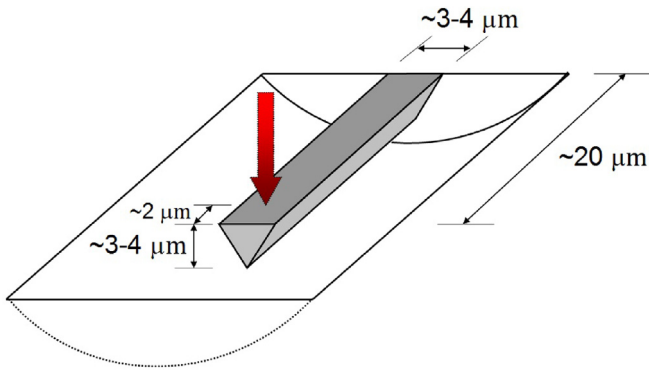


Fig. 1. Scheme of a cantilever micro-beam. An arrow shows loading direction.

of ion damage on the mechanical properties of the specimens in the micrometer range is expected to be negligible [30]. Considering fast scanning of ion beam over the milled area and thermal conductivity of cement paste $\approx 1 \text{ Wm}^{-1} \text{ K}^{-1}$, an approach based on Melngailis [31] and Ishitani and Kaga [32] gives maximum temperature rise at the surface several tens of degrees. For this reason we also do not expect substantial thermally activated microstructural changes in the volume of the micro-beams. However, the sample is exposed to high vacuum and some unavoidable C-S-H gel shrinkage can be anticipated.

2.3. Details of micro-beam fabrication

At first, the sample surface was carefully analyzed by SEM and locations of individual microscopically distinguishable phases with a sufficient extent were found. The inner product (mainly C-S-H_{HD} mixed with other hydrates) occurs mainly as rims around anhydrous clinker particles or is located at the places of former clinker grains past full hydration [6]. The phase is characterized by dark gray color in the back-scattered electron (BSE) mode of SEM micrographs. An example of a micro-beam fabricated in the inner product is shown in Fig. 2. Places of lighter gray color with visible submicron porosity are characteristic of the outer product (mainly C-S-H_{LD} regions mixed with other hydrates). The outer product regions free of other phases (like CH or clinker remnants) are relatively rare in the microstructure. An example of such a place and resulting micro-beam after FIB milling are shown in Fig. 3. The terms inner and outer products are coined from cement chemistry [5,6] and relate to the mixture of C-S-H gels with other hydrates (e.g. AFt, AFm, C-A-H) that form in the close vicinity of a clinker (inner product) and further from clinkers (outer product). Large areas of the CH phase suitable for the fabrication of 20 μm long

micro-beams are frequently found in the cement paste microstructure as illustrated in Fig. 4. The geometry of the micro-beams was carefully measured in SEM and the final number of the best 8–11 pieces for each phase was prepared.

2.4. Micro-bending tests

The micro-bending test was instrumented with the nano-indenter. The in-situ imaging technique of the Hysitron Tribolab system was used to locate the point of loading on the micro-beam. The technique uses a piezo-scanner with subnanometer precision and the Berkovich tip for the surface scanning. The point of loading was always located in the centerline of the top cantilever surface and around 2 μm from its free end (Fig. 1).

The loading protocol contained two stages. Firstly, the indenter tip was brought to contact and loaded in three cycles (load controlled) in a fully elastic regime. The maximum applied load was 60 μN for the inner product and 30 μN for the outer product and CH, respectively, in this stage. Each loading cycle was composed of a 5 s loading, 5 s holding and 5 s unloading period (Fig. 5). It can be seen from Fig. 5 that all the three phases behave perfectly elastically in the given loading range (see the overlapping cycles in Fig. 5 a). The stage served for the evaluation of the phase Young's modulus from

$$E = \frac{F_e L^3}{3w_e I_y} \quad (1)$$

where F_e and w_e are the force and deflection reached in the elastic regime, respectively (measured by the nanoindenter), L is the micro-beam length (point of indenter's contact to the breaking point on the cantilever), $I_y = \frac{1}{36}bh^3$ is the second moment of inertia with b and h being the width and the depth of the triangular cross section (measured by SEM). The value was compared to the values obtained from the indents performed in the close vicinity of the micro-beam. The indentation was carried out with the same loading conditions as applied in the grid nanoindentation (Section 2.5). The number of indents was 5–10 and characteristics evaluated by the Oliver and Pharr method [33] can be considered as direct estimates of the micro-beam elastic modulus.

In the second stage, the micro-beam was progressively loaded by a constant displacement increment (50 nm/s) up to the failure. The maximum reached force was used for the tensile strength calculation using the elastic theory of beams as

$$f_t = \frac{F_{max} L}{I_y} \frac{h}{3} \quad (2)$$

where F_{max} is the maximum force (measured by the nanoindenter). Note, that only pure bending effects were considered in Eqs. (1) and

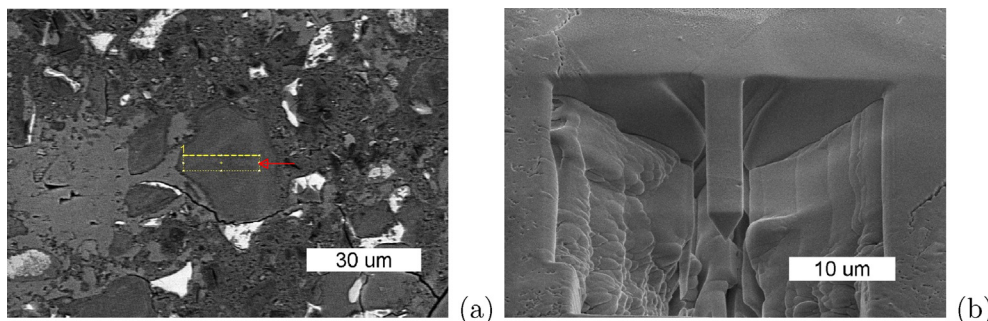


Fig. 2. Cantilever micro-beam fabricated in the inner product. (a) Location before FIB milling labeled by the yellow rectangle. The red arrow indicates the fixed end position. (b) Front view of the cantilever after FIB milling. (For interpretation of the references to color in this figure legend, the reader is referred to the web version of this article.)

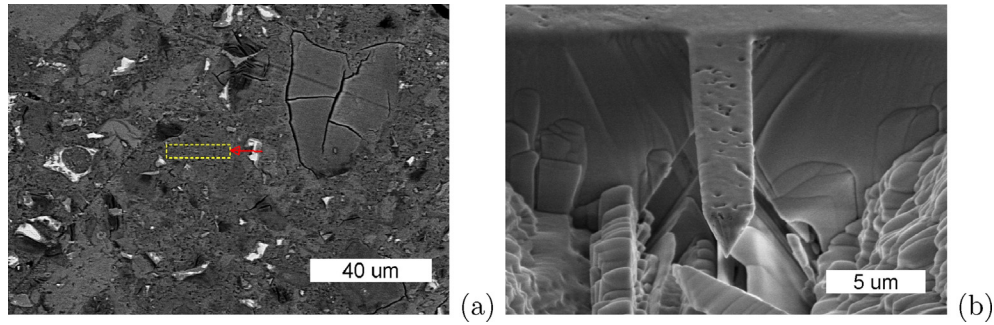


Fig. 3. Cantilever micro-beam fabricated in the outer product. (a) Location before FIB milling labeled by the yellow rectangle. The red arrow indicates the fixed end position. (b) Front view of the cantilever after FIB milling. (For interpretation of the references to color in this figure legend, the reader is referred to the web version of this article.)

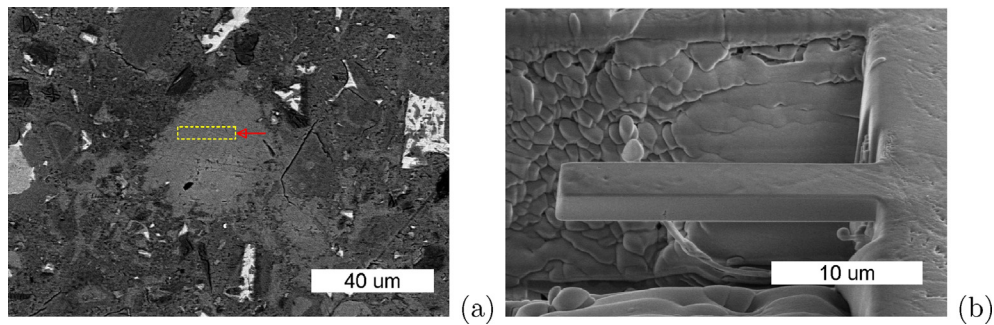


Fig. 4. Cantilever micro-beam fabricated in CH. (a) Location before FIB milling labeled by the yellow rectangle. The red arrow indicates the fixed end position. (b) Side view of the cantilever after FIB milling. (For interpretation of the references to color in this figure legend, the reader is referred to the web version of this article.)

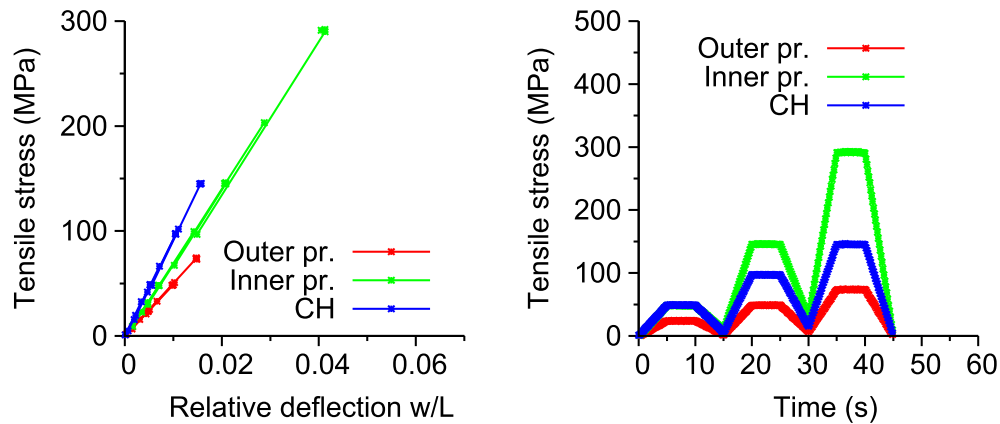


Fig. 5. Cyclic loading in the elastic regime. Tensile stress versus relative beam deflection diagrams (w , and L stand for the beam deflection and length, respectively) and the course of cyclic loading.

(2) since the small beam depth to length ratio allows neglecting the effect of shear forces. The ratio of the deflection caused by the shear force to the deflection caused by bending is 0.005 for our micro-beam dimensions, thus the shear effect is negligible. The susceptibility to the brittle failure of the beams was quantified by the supremum estimate of the total fracture energy computed as

$$G_f^{sup} = \frac{1}{A_f} \int_0^{w_{max}} Fdw \quad (3)$$

where F is the force, w_{max} is the peak deflection and A_f is the fracture area. The supremum fracture energy is computed from the

assumption that the micro-beam behavior shows neither snap-back nor softening and that the maximum force corresponds to the maximum energy release rate with a limiting stable crack propagation. The fracture area was approximated by the whole ligament area which, for a triangular cross section without a notch, yields $A_f = \frac{1}{2}bh$.

2.5. Grid nanoindentation

Micromechanical characterization of the sample was provided by grid nanoindentation. The technique is capable of the assessment of both phase elasticity and hardness and volume fraction estimates from load-displacement diagrams measured from the

impression of a sharp tip. Although it is possible to derive single phase properties directly using a combination of SEM-EDS and nanoindentation (e.g. Ref. [34]) this approach was not applied here since it requires SEM imaging and EDS microanalysis of each indent and it is time consuming. The intention of using grid nanoindentation was to provide estimates on the statistical distribution of phases' properties over a large sample surface area rather than exact specification of a single phase properties. Thus, the later applied deconvolution (Section 3.4) indicates an approximate phase volumetric content, ratios between the phases and the estimation of phase elastic stiffness with a sufficient precision for the purposes of this work.

The analysis was performed with the Hysitron Tribolab HI-700 system equipped with a sharp three-sided pyramidal (Berkovich) tip. Five grids each containing 10×10 indents (i.e. covering a $300 \times 300 \mu\text{m}^2$ area) on arbitrarily chosen sample locations were performed to cover the area of the sample containing a representative amount of all the phases. The $30 \mu\text{m}$ separation between individual indents and small applied loads secure a negligible mechanical influence between the neighboring spots. The indents were load controlled with the maximum indentation force of 2 mN leading to average maximum penetration depths ≈ 250 nm. This choice ensures that the indentation affected volume lies within a distinct phase and the assumption of a homogeneous-like volume can be used for the evaluation of elastic constants [18]. The loading diagram contained three segments: linear loading lasting for 5 s, a 20 s holding period (to minimize the effect of creep on elastic constants derived from the unloading branch [11]) and a 5 s unloading segment. The Oliver and Pharr theory [33] was used to derive the reduced modulus:

$$E_r = \frac{1}{2\beta} \frac{\sqrt{\pi}}{\sqrt{A_c}} \left. \frac{dP}{dh} \right|_{h=h_{max}} \quad (4)$$

where dP/dh is the contact stiffness assessed as the slope of the indentation unloading branch at the maximum depth h_{max} , A_c is the projected contact area of the tip at peak load, and β is the geometrical correction factor introduced to correct the non-symmetrical indenter shape ($\beta = 1.034$ for the Berkovich tip). The effect of non-rigid indenter was taken into consideration by the following equality

$$\frac{1}{E_r} = \frac{1 - \nu^2}{E} + \frac{1 - \nu_i^2}{E_i} \quad (5)$$

where E and ν correspond to the elastic modulus and Poisson's ratio of the tested material, respectively. E_i and ν_i are the parameters of the indenter ($E_i = 1141$ GPa and $\nu_i = 0.07$ for diamond). Another material quantity, the hardness H , representing the mean contact pressure under the indenter can readily be obtained from load-penetration indentation curves as

$$H = \frac{P}{A_c} \quad (6)$$

3. Results

3.1. SEM analysis

Ratios between the volumetric amount of individual phases in cement paste were estimated by image analysis from segmented SEM images taken in the BSE mode. 32 images (with resolution of 1024×943 pixels) from arbitrary locations of the specimen surface

(areas of $\approx 150 - 200 \times 150 - 200 \mu\text{m}^2$) were taken and evaluated using common pixel color intensity thresholds for all images. Four phases were separated, namely porosity, hydrates (note: there is a smooth transition between the pixel luminosities of hydrates, so no distinction between inner and outer products and other hydrates was performed) and clinker minerals. The thresholds (for pores and clinkers) were based on local minima in grayscale luminosity histograms (Fig. 6). The CH phase can be detected morphologically as large crystals in Fig. 6 a. However, a portion of CH is well below the resolution limit of the image analysis, so the real CH volume fraction was not approached.

The example of the analyzed, segmented and processed image is shown in Fig. 6. The overall results of volume fractions received from this analysis are summarized in Table 2. Note, that due to the resolution limits of the images, objects (pores in this case) smaller than $\approx 0.1 \mu\text{m}$ could not be detected. Therefore, this fact must be taken into account when interpreting the results from Table 2 and the real overall porosity of the sample must be expected to be (much) higher.

3.2. MIP porosimetry

The specimen was crushed to the size of a few millimeters, dried at 105°C for six hours and intruded by mercury (MIP, Autopore III, Micromeritics). The bulk density reached the value of 1.867 g/cm^3 and the total pore volume was 14.51%. The Mercury Intrusion Porosimetry (MIP) has its resolution limits (in terms of pore diameters) around ≈ 10 nm in the bottom and $\approx 10 \mu\text{m}$ at the top meaning no much larger capillary pores can be detected by this method. Image analysis provides a better estimate of large capillary pores in this particular case (see Section 3.1).

The pore diameter distribution was calculated by the classical Washburn's theory from mercury pressures assuming cylindrical pore geometry. The majority of the micropores lies below 100 nm as can be seen in Fig. 7.

3.3. Volume fractions from CEMHYD3D model

The 3D model [35] that is devoted to the simulation of the hydration process and the development of a hydrated cement microstructure was applied to the assessment of volume fractions of individual chemical phases within the tested samples. The oxide composition from Table 1 was recalculated to clinker minerals according to the Taylor formula [5]. The results yielded: C_3S 64.35%, C_2S 11.81%, C_3A 3.99%, C_4AF 11.87% and gypsum 5.53% by volume. The amount of unhydrated clinker 3.4% vol. obtained by SEM corresponds to the degree of hydration equal to 0.918. This results in volume fractions of CH 19.6%, C-S- H_{LD} 24.9%, C-S- H_{HD} 24.8%, other hydrates 15.2% and capillary porosity 12.1%.

The SEM-based image analysis underestimates the capillary porosity by a large amount (only 2.9% compared to 12.1% in CEM-HYD3D), which also yields an overestimation in the hydrates content. Unfortunately, the SEM analysis on this resolution cannot distinguish finer capillary pores which are intermixed with hydrates. The reason lies in the resolution limits of the method as explained in Section 3.1. On the other hand, the MIP porosity of 14.51% is consistent with the simulation result, considering a partial overlap between the capillary and gel pores.

3.4. Grid nanoindentation

The methodology described in Section 2.5 was applied to nanoindentation data with the assumption of a constant Poisson's ratio of 0.2 for all the phases without losing much precision since any reasonable estimate of the ratio typical of cement minerals and

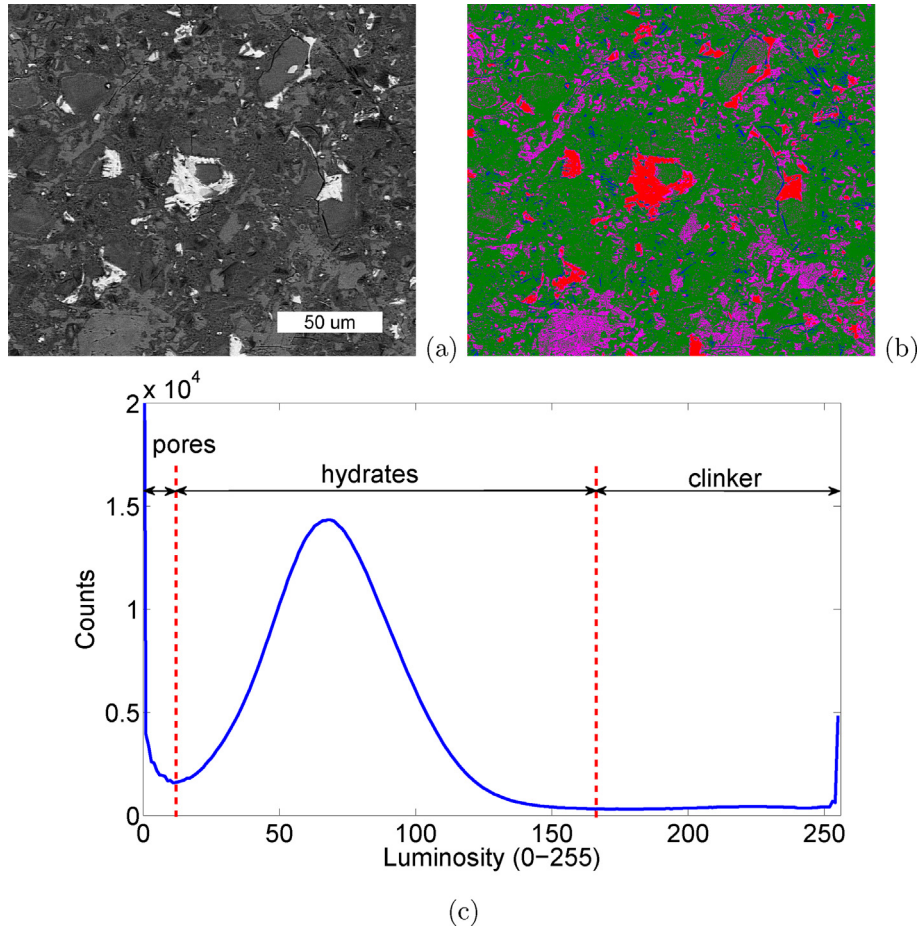


Fig. 6. Image analysis of the cement paste microstructure and performed phase segmentation. (a) Original SEM-BSE image. (b) Segmented image (blue = pores; green + violet = hydrates (violet = large CH crystals as a part of hydrates); red = clinker) and (c) averaged luminosity histogram (from 32 images) with phase thresholds. (For interpretation of the references to color in this figure legend, the reader is referred to the web version of this article.)

Table 2
Results of phase segmentation by image analysis.

Component	Pores	Hydrates	Clinker
Content	2.9 ± 1.8 %	93.7 ± 3.1 %	3.4 ± 1.8 %

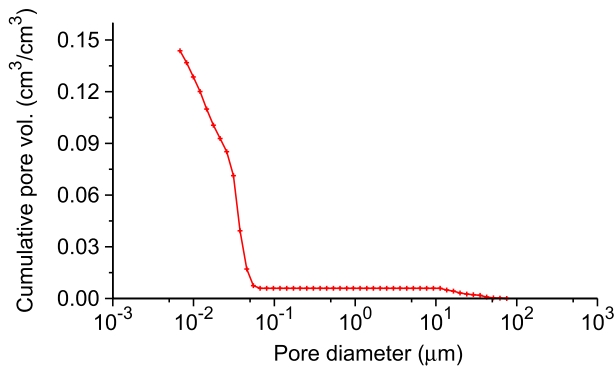


Fig. 7. Cumulative pore volume measured by MIP.

products (0.15–0.25) leads to very similar results using Eq. (5). The frequency plots of elastic moduli and the hardness merged from all positions (500 indents) are shown in Fig. 8. It can be seen in Fig. 8

that the histogram is relatively smooth with one significant peak (belonging to the prevailing C-S-H phases possibly mixed with other hydrates) and some minor peaks belonging to the rest of the phases. To quantify the differences between the phases their characteristic Young's moduli and volume fractions were estimated by the statistical deconvolution [16,18,20]. In this method, the results in the form of frequency plots are analyzed so that the minimization procedure seeks parameters of several Gauss distributions in an experimental probability density function (PDF), see Fig. 9. In the deconvolution algorithm, a random seed and minimizing criteria based on deviations between the experimental and theoretically computed overall PDFs are calculated to find the best fit given by a quadratic norm. The non-uniqueness of the solution is overcome by fixing the number of searched phases to a finite number. The bin size used for the construction of the E-moduli histogram in Fig. 9 was set to 1 GPa. Details on the deconvolution procedure can be found in Refs. [20,16].

The deconvolution procedure was only applied to a portion of the data with Young's moduli of 10–55 GPa because: (i) pores with zero stiffness cannot be sensed by nanoindentation and their volume is better estimated from image analysis or MIP and (ii) hard particle (clinker) stiffness and volume fraction is not assessed well by indentation in a composite with a compliant matrix (when the stiffness mismatch ratio is more than 4 [18]) and it is better to measure the clinker's stiffness out of the composite [10,11]. Therefore, the number of searched phases was fixed to three,

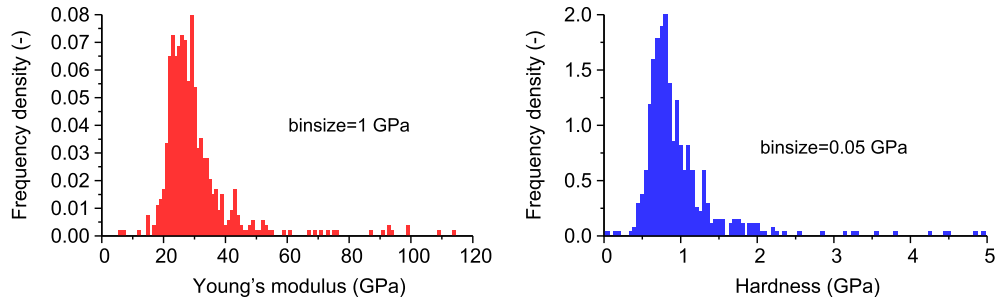


Fig. 8. Frequency plots of Young's moduli and hardness from nanoindentation.

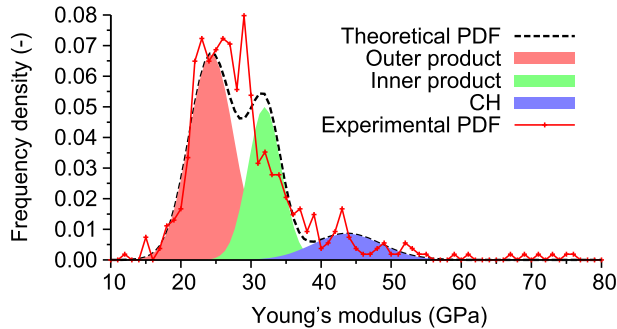


Fig. 9. Frequency plots of Young's moduli with deconvoluted phase distributions.

namely the outer product, inner product and CH. Note that the deconvolution procedure seeks for mechanically dissimilar phases within the frequency plots rather than chemically distinct phases so the direct comparison of the deconvolution with SEM-based image analysis or CEMHYD3D simulations is not straightforward. Note also that, as already mentioned, the indentation volume as well as the volume of microbeams may include a mixture of chemically pure phases. The grid indentation is used to give an idea what is the volumetric content of the mechanically dissimilar phases tested later by the beam bending. Other approaches based on e.g. focussed-ion beam nanotomography [36] may lead to higher resolution in separation of the phases. Nevertheless, the analyses are in very close agreement for the given case, see Tables 2 and 3 and analyses comparison in Table 4. Young's moduli presented in Table 3 are also in very good agreement with the literature data [18,19,34].

3.5. Micro-bending tests

The tensile stress (evaluated at the top edge of the breaking cross-section as $\sigma_t = \frac{F L}{I_y \frac{h}{3}}$) versus relative beam deflection diagrams for all phases are depicted in Fig. 10. It can be seen in the figure that the micro-beams of all phases deviate very little from the elastic response even before breaking after which the measurement is unstable and the force drops down to zero without control.

Table 3
Results of phase deconvolution from nanoindentation.

Phase	Young's modulus (GPa)	Volume fraction
Pores	0	0.121*
Outer product	24.4 ± 3.2	0.499
Inner product	31.9 ± 2.4	0.279
CH	43.7 ± 4.9	0.098
Clinkers	121.0 ± 14.0 [†]	0.034*

Note: * from CEMHYD3D; [†] from Ref. [11].

The tensile strengths (i.e. maximum tensile stresses) and supremum fracture energies reached during the cantilever bending are summarized in Table 5 together with elastic properties of the phases measured by micro-beam bending and nanoindentation.

The fracture surfaces are shell-like and smooth for fractured CH micro-beams (Fig. 11 a). On the contrary, the fracture surface in the outer product micro-beam is rougher dictated by the inner capillary porosity which penetrates through the tested volume (Fig. 11b). Since the micro-beams were fabricated as unnotched the breaking point was typically not exactly at a fixed point but a few micrometers away in the cantilever where it was initiated by a random geometrical or material imperfection (typically a pore).

4. Discussion

The performed measurement of the elastic properties of individual cement paste phases was validated through both nanoindentation and micro-beam bending tests (Fig. 5a and Table 5). The agreement between the methods shows that correct assumptions were used and minimum geometrical imperfections were introduced by the FIB technique. The mean values of Young's moduli of individual phases also agree very well with the statistical grid indentation performed in this paper (Section 2.5) and with the literature results [13,18].

The deformation of micro-beams was found to be mostly linearly elastic almost till the breaking point for all the phases (Fig. 10). The failure occurred suddenly in a brittle manner. Low supremum fracture energies G_f^{sup} were found for all the phases, especially for the outer product (4.4 J/m², Table 5). Higher, but still small, supremum fracture energies were assessed for the inner product and CH (19.7 – 19.9 J/m², Table 5). The determination of a real fracture energy would need testing smaller samples where the stored elastic energy at the maximum force is below the real G_f and the softening part would then emerge in Fig. 10 instead of an unstable strength loss. Since this was not the case, the instrument was unable to capture the load-displacement correctly after the peak (even using displacement control), which was manifested by a sudden drop in force (Fig. 10).

Ghebrab and Soroushian [37] found that the fracture energy of (C-S-H)-(C-S-H) debonding lies in the interval of 0.38 – 2.85 J/m² and the CH crystal pullout raises these values to 16.9 – 283 J/m². Bauchy et al. [38] estimated the fracture energy of C-S-H as 1.72 ± 0.29 J/m² from molecular dynamics without any pull-out mechanism. Further experiments are needed to cover these effects and justify the theoretical predictions.

The variation in the strength of the phases is relatively low for inner and outer products compared to CH, which might be caused by the crystalline and anisotropic nature of CH compared to amorphous (and statistically isotropic) hydrates. Nevertheless, the mean strengths of the inner product and CH are comparable

Table 4
Comparison of volume fractions (in %) estimated by SEM image analysis, MIP, CEMHYD3D model and grid nanoindentation with deconvolution.

Image analysis	pores	hydrates	clinker
	2.9 ± 1.8	93.7 ± 3.1	3.4 ± 1.8
MIP	pores		
	14.5		
CEMHYD3D	pores	C-S-H _{LD} C-S-H _{HD} CH other	clinker
	12.1	24.9 24.8 19.6 15.2	3.4
grid NI	pores	outer p. inner p. CH	clinker
	12.1*	49.9 27.9 9.8	3.4*
		Sum=84.5	
		Sum=87.6	

Note: grid NI = grid nanoindentation and deconvolution; * from CEMHYD3D.

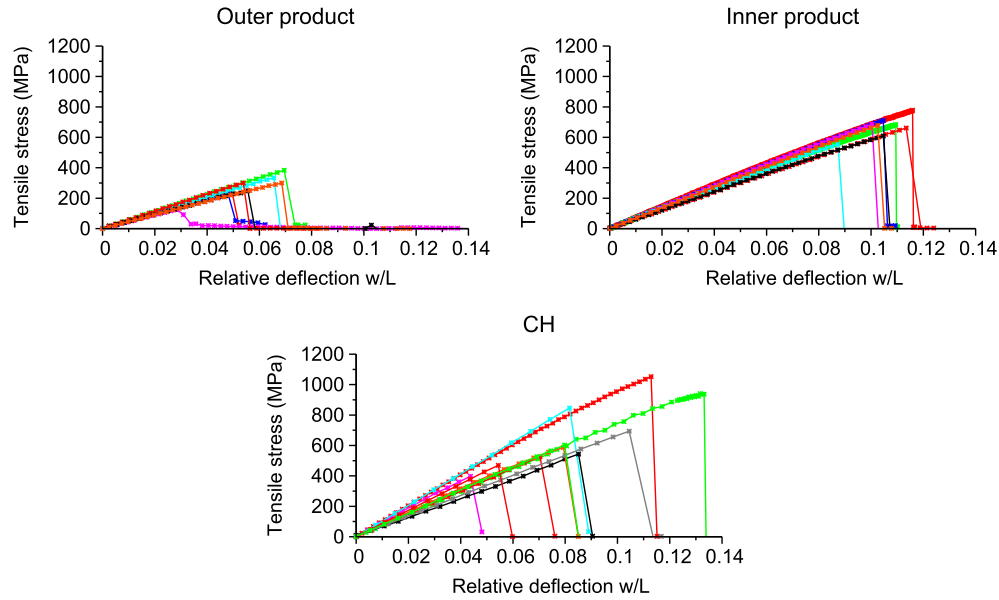


Fig. 10. Tensile stress versus relative beam deflection curves for specific phases measured in the micro-bending test (w , and L stand for beam deflection and length, respectively).

(means 655 – 700 MPa, Table 5) whereas the outer product's strength is much lower (mean 264 MPa, Table 5) being about 40% of the CH strength. From the grid nanoindentation and deconvolution, the volumetric content of the outer product is comparable to the inner product plus CH (0.499:0.377) but the weakest link in the chain is still the outer product with the highest content, the lowest strength and the lowest fracture energy.

In general, the tensile strength of the micro-level components might seem to be very high compared to the macroscopic values of cement paste's strength (measured at the millimeter level), which is typically only a few MPa. The simplest formula for the theoretical

tensile strength originates from breaking atomic bonds and pulling both parts apart as

$$f_t^{theor} = \sqrt{\frac{E\gamma}{a_0}} \tag{7}$$

where E is Young's modulus, γ is the fracture surface energy and a_0 is the interatomic spacing. Typical estimates are $f_t^{theor} \in (0.01 - 0.10) E$ [39,40]. This gives a theoretical tensile strength of C-S-H_{LD} in the range $f_t^{theor} \in (239 - 2390)$ MPa, which already coincides with our experimental results.

Molecular dynamics models try to predict cement strength properties from lower level characteristics of its basic building blocks, C-S-H globules. The tensile strength of the globules is estimated from 1 to 3 GPa depending on dry or wet conditions [41]. However, such a high value has never been observed on higher length scales due to the presence of multiple structural defects and phase interactions.

The multiscale model developed by Hlobil et al. [7,8] for cement paste identified the tensile strength of C-S-H_{LD} to be 66 MPa by means of inverse analysis. This value is 264/66 = 4 times lower than that measured experimentally in this paper. The most probable explanation of this discrepancy is that simplified morphology of the C-S-H foam is used by the model. The model assumes spatial distribution of the C-S-H only between two cement grains while the failure surface in reality passes through regions among several

Table 5
Elastic properties, hardness, tensile strengths and fracture energies of individual phases from micro-beam bending tests and from nanoindentation in the vicinity of micro-beams.

	Test type	Phase		
		Outer product	Inner product	CH
E (GPa)	BB	23.9 ± 1.4	34.0 ± 1.9	39.2 ± 6.6
	NI	24.9 ± 1.3	33.6 ± 2.0	39.0 ± 7.1
H (GPa)	NI	0.98 ± 0.07	1.15 ± 0.11	1.37 ± 0.11
f_t (MPa)	BB	264.1 ± 73.4	700.2 ± 198.5	655.1 ± 258.3
G_f^{sup} (J/m ²)	BB	4.4 ± 1.9	19.7 ± 3.8	19.9 ± 14.4
No. of tests		8	8	11

Legend: E = Young's modulus; H = hardness; f_t = tensile strength; G_f^{sup} = supremum of fracture energy; NI = nanoindentation tests performed in the vicinity of the micro-beam; BB = beam bending.

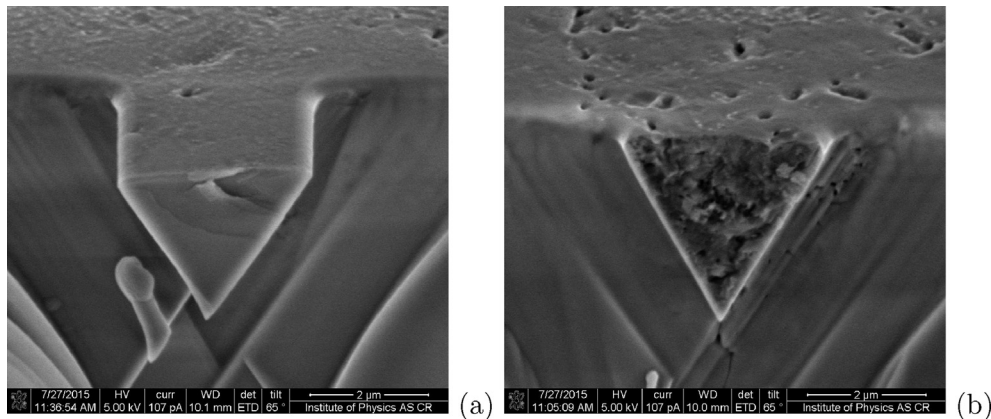


Fig. 11. SEM micrograph of the fracture surface on (a) CH and (b) outer product micro-beams.

grains, taking into account the weakest link in the microstructure. Other minor reasons could include partial heterogeneous micro-beam composition or partial carbonation. It is worthy to mention that the compressive/tensile uniaxial strength yields a constant ratio 8 according to the Griffith model [42], which gives compressive strength $264 \times 8 = 2112$ MPa for C-S-H_{LD}.

Chen et al. [25] reported tensile strength of a single FIB machined micro-beam with rhomboidal cross section to be 2.67 MPa which seems to be in contradiction (as indicated in the introduction) to scaling of strength to micrometers in quasi-brittle materials [26]. The beam used for the bending test had width of $3.5 \mu\text{m}$ and length of $5 \mu\text{m}$. The displacement recorded with AFM reached just about 15 nm and the corresponding force was about 0.8 μN which is only as large as the contact force of the nano-indenter. The load-deflection curve was characterized by some excursions which were left without explanations. Although authors do not present the Young's modulus E computed from beam bending it can be reproduced from their results. This reproduction leads to the range of $E \in (0.09; 0.13)$ GPa which is unreasonably low (two orders of magnitude). Therefore, we do not take the results into considerations.

Despite the very high tensile strength of the microscale phases measured in this paper, it can be readily hypothesized that other defects like large capillary porosity, cracks (e.g. due to thermal or shrinkage strains) and stress concentrators (clinkers) have a direct influence on the strength decrease on higher scales compared to the tested micrometer level [8].

5. Conclusions

The paper shows the results of nanoindentation driven measurements of cantilever micro-beams fabricated by FIB in distinct microscale phases of hydrated cement paste. This pioneering work in the area was motivated by the results given by multi-scale and molecular dynamics models that predict very high values of C-S-H tensile strength. The observation level was chosen to be in micrometer range where distinct microscale phases like inner and outer products and Portlandite can be distinguished and micro-beams well fabricated by FIB. The microstructure of the phases at this level also contains a portion of gel and capillary porosity which was quantified by MIP as 14.51% with the majority of pore diameters below 100 nm. It was possible to fabricate micro-beams by FIB without any significant geometrical defects and the ion interaction was found to be negligible compared to the tested specimen dimensions. The only unavoidable deteriorating effect was the drying shrinkage of hydrates exposed to high vacuum. Nanoindentation

successfully served both for the derivation of hydrated cement's mechanical properties and a micro-compression tool for beam bending.

Based on the performed experiments, the following particular conclusions can be drawn.

1. The tensile deformation of hydrated cement phases at the micrometer scale is almost purely elastic up to their brittle failure.
2. The Young's moduli measured by nanoindentation and evaluated from bending tests agree very well for all tested phases.
3. The tensile strength of the phases at the micrometer level was found to be by two orders of magnitude higher compared to the macroscopic values of cement pastes. The mean tensile strengths were in the range of 264 MPa (for the outer product) to 700 MPa (for the inner product and CH).
4. Low supremum fracture energies were detected for the tested phases at the microscale (4.4 J/m^2 for the outer product and $\approx 20 \text{ J/m}^2$ for the inner product and CH).
5. The experimentally obtained values of tensile strengths and fracture energies are in close agreement with the results predicted by molecular dynamics models (using the bottom-up approach) and multiscale models (using the inverse top-down approach) found in the recent literature.

Acknowledgement

The authors from the Faculty of Civil Engineering (J. Němeček, V. Králík and V. Šmilauer) would like to acknowledge support offered by the Czech Science Foundation (project No. 16-11879S). The authors from the Institute of Physics (L. Polívka and A. Jäger) would like to acknowledge support offered by the Centre of Excellence (project No. GBP108/12/G043). The authors would like to thank J. Bočan and J. Maňák from the Institute of Physics for their support with the measurement and evaluation.

References

- [1] P.K. Mehta, P.J.M. Monteiro, *Concrete: Microstructure, Properties, and Materials*, fourth ed., McGraw-Hill, 2014.
- [2] O. Bernard, F.-J. Ulm, E. Lemarchand, A multiscale micromechanics-hydration model for the early-age elastic properties of cement-based materials, *Cem. Concr. Res.* 33 (9) (2003) 1293–1309.
- [3] J. Vorel, V. Šmilauer, Z. Bittnar, Multiscale simulations of concrete mechanical tests, *J. Comput. Appl. Math.* 236 (18) (2012) 4882–4892.
- [4] L. Sorelli, G. Constantinides, F.-J. Ulm, F. Toutlemonde, The nano-mechanical signature of ultra high performance concrete by statistical nanoindentation techniques, *Cem. Concr. Res.* 38 (12) (2008) 1447–1456.
- [5] H. Taylor, *Cement Chemistry*, second ed., Thomas Telford, 2003.

- [6] K.L. Scrivener, Backscattered electron imaging of cementitious microstructures: understanding and quantification, *Cem. Concr. Compos.* 26 (8) (2004) 935–945 scanning electron microscopy of cements and concretes.
- [7] M. Hlobil, V. Šmilauer, Microstructure-based micromechanical model for compressive strength evolution of cement paste, in: S. Bernal, J. Provis (Eds.), *Proceedings of 34th Annual Cement and Concrete Science Conference*, University of Sheffield, Sheffield, 2014.
- [8] M. Hlobil, V. Šmilauer, G. Chanvillard, Micromechanical multiscale fracture model for compressive strength of blended cement pastes, *Cem. Concr. Res.* 83 (2016) 188–202.
- [9] A.C. Fischer-Cripps, *Nanoindentation*, Springer, 2002.
- [10] K. Velez, S. Maximilien, D. Damidot, G. Fantozzi, F. Sorrentino, Determination by nanoindentation of elastic modulus and hardness of pure constituents of Portland cement clinker, *Cem. Concr. Res.* 31 (2001) 555–561.
- [11] J. Němeček, Creep effects in nanoindentation of hydrated phases of cement pastes, *Mater. Charact.* 60 (2009) 1028–1034.
- [12] P. Tennis, H. Jennings, A model for two types of calcium silicate hydrate in the microstructure of portland cement pastes, *Cem. Concr. Res.* 30 (2000) 855–863.
- [13] G. Constantinides, F.-J. Ulm, The effect of two types of c-s-h on the elasticity of cement-based materials: results from nanoindentation and micromechanical modeling, *Cem. Concr. Res.* 34 (1) (2004) 67–80.
- [14] M. Vandamme, F.-J. Ulm, Viscoelastic solutions for conical indentation, *Int. J. Solids Struct.* 43 (10) (2006) 3142–3165.
- [15] P. Mondal, S.P. Shah, L.D. Marks, Nanoscale characterization of cementitious materials, *Mater. J.* 105 (2) (2008) 174–179.
- [16] J. Němeček, V. Králík, J. Vondřejc, Micromechanical analysis of heterogeneous structural materials, *Cem. Concr. Compos.* 36 (0) (2013) 85–92.
- [17] C. Hu, Z. Li, A review on the mechanical properties of cement-based materials measured by nanoindentation, *Constr. Build. Mater.* 90 (0) (2015) 80–90.
- [18] G. Constantinides, K.R. Chandran, F.-J. Ulm, K.V. Vliet, Grid indentation analysis of composite microstructure and mechanics: principles and validation, *Mater. Sci. Eng. A* 430 (12) (2006) 189–202.
- [19] F.-J. Ulm, M. Vandamme, M. Bobko, J. Ortega, Statistical indentation techniques for hydrated nanocomposites: concrete, bone, and shale, *J. Am. Ceram. Soc.* 90 (9) (2007) 2677–2692.
- [20] J. Němeček, V. Šmilauer, L. Kopecký, Nanoindentation characteristics of alkali-activated aluminosilicate materials, *Cem. Concr. Compos.* 33 (2) (2011) 163–170.
- [21] P. Trtik, J. Kaufmann, U. Volz, On the use of peak-force tapping atomic force microscopy for quantification of the local elastic modulus in hardened cement paste, *Cem. Concr. Res.* 42 (1) (2012) 215–221.
- [22] M.L. Palacio, B. Bhushan, Depth-sensing indentation of nanomaterials and nanostructures, *Mater. Charact.* 78 (0) (2013) 1–20.
- [23] J. Gong, A.J. Wilkinson, Micro-cantilever testing of <a> prismatic slip in commercially pure Ti, *Philos. Mag.* 91 (7–9) (2011) 1137–1149.
- [24] E. Schlangen, M. Lukovic, B. avija1, O. Copuroglu, Nano-indentation testing and modelling of cement paste, in: C.H. abd Bernhard Pichler, J. Kollegger (Eds.), *Proceedings of the 10th International Conference on Creep, Shrinkage, and Durability of Concrete and Concrete Structures*, Reston, Virginia, American Society of Civil Engineers, Vienna, Austria, 2015.
- [25] S.J. Chen, W.H. Duan, Z.J. Li, T.B. Sui, New approach for characterisation of mechanical properties of cement paste at micrometre scale, *Mater. Des.* 87 (2015) 992–995.
- [26] Z. Bazant, *Scaling of Structural Strength*, second ed., Elsevier Ltd., 2005.
- [27] L. Gianuzzi, F. Stevie, *Introduction to Focused Ion Beams. Instrumentation, Theory, Techniques and Practice*, Springer, 2005.
- [28] D.E. Armstrong, A.J. Wilkinson, S.G. Roberts, Measuring anisotropy in young's modulus of copper using microcantilever testing, *J. Mater. Res.* 24 (2009) 3268–3276.
- [29] J. Ziegler, *The Stopping and Range of Ions in Matter - SRIM*, 2013. <http://www.srim.org>.
- [30] D. Kiener, C. Motz, M. Rester, M. Jenko, G. Dehm, Fib damage of cu and possible consequences for miniaturized mechanical tests, *Mater. Sci. Eng. A* 39 (17) (2007) 262–272.
- [31] M.J., Critical review: focused ion beam technology and applications, *J. Vac. Sci. Technol. B* 5 (2) (1987) 469–495.
- [32] I. T., K. H., Calculation of local temperature rise in focused ion beam sample preparation, *J. Electron Microsc.* 44 (1995) 331–336.
- [33] W. Oliver, G. Pharr, An improved technique for determining hardness and elastic modulus using load and displacement sensing indentation experiments, *J. Mater. Res.* 7 (1992) 1564–1583.
- [34] J.J. Hughes, P. Tirtik, Micro-mechanical properties of cement paste measured by depth-sensing nanoindentation: a preliminary correlation of physical properties with phase type, *Mater. Charact.* 53 (2–4) (2004) 223–231.
- [35] D.P. Bentz, Quantitative comparison of real and CEMHYD3D model microstructures using correlation functions, *Cem. Concr. Res.* 36 (2) (2006) 259–263.
- [36] P. Lura, P. Trtik, B. Mnch, Validity of recent approaches for statistical nano-indentation of cement pastes, *Cem. Concr. Compos.* 33 (4) (2011) 457–465.
- [37] T. Ghebrab, P. Soroushian, Mechanical properties of hydrated cement paste: development of structure-property relationships, *J. Concr. Struct. Mater.* 7 (4) (2010) 37–43.
- [38] M. Bauchy, H. Laubie, M.A. Qomi, C. Hoover, F.-J. Ulm, R.-M. Pellenq, Fracture toughness of calcium-silicate-hydrate from molecular dynamics simulations, *J. Non Cryst. Solids* 419 (2015) 58–64.
- [39] D.K. Felbeck, A.G. Atkins, *Strength and Fracture of Engineering Solids*, Prentice-Hall, New Jersey, 1984.
- [40] H. Gao, Application of fracture mechanics concepts to hierarchical biomechanics of bone and bone-like materials, *Int. J. Fract.* 138 (1–4) (2006) 101–137.
- [41] R.J.-M. Pellenq, A. Kushima, R. Shahsavari, K.J.V. Vliet, M.J. Buehler, S. Yip, F.-J. Ulm, A realistic molecular model of cement hydrates, *Proc. Natl. Acad. Sci. U. S. A.* 106 (38) (2009), 1610216107.
- [42] A. Griffith, Theory of rupture, in: C. Biezeno, J. Burgers (Eds.), *First International Congress for Applied Mechanics*, Delft, 1924, pp. 55–63.